Computational Geosciences (2021) 25:2005–2017
https://doi.org/10.1007/s10596-021-10077-8

ORIGINAL PAPER

Effective viscoelastic representation of gas-hydrate bearing sediments from finite-element harmonic experiments

Juan E. Santos[1,2,3] · Patricia M. Gauzellino[4] · José M. Carcione[1,5] · Jing Ba[1]

Accepted: 15 July 2021 / Published online: 16 August 2021

Abstract

We present a novel numerical upscaling technique for modeling the wave response of gas-hydrate bearing sediments composed of a rock frame, gas-hydrate and water, where the hydrate consists of ice-like lattice of water molecules with methane trapped inside. These sediments are highly heterogeneous at mesoscopic scales, much smaller than the wavelength but much larger than the pore size, inducing substantial seismic wave attenuation and dispersion due to mode conversions. The proposed numerical upscaling procedure simulates the wave-induced fluid-flow loss mechanism by computing an average effective viscoelastic medium having the same behavior of the original sediment. The method determines the complex stiffness coefficients associated with the viscoelastic medium by solving numerically boundary value problems formulated in the space-frequency domain, representing compressibility and shear experiments. The procedure is applied to composite media with regions of different amounts of hydrate with patchy or periodic-layer distributions, which define an anisotropic effective viscoelastic medium, respectively. The examples demonstrate that variations in hydrate content induce strong attenuation and dispersion effects on seismic waves due to the mesoscopic loss mechanism.

Keywords Gas-hydrate sediments · Finite elements · Wave-induced fluid flow attenuation · Seismic velocity

Mathematics Subject Classification (2010) 35Q86 · 35D30 · 65N30

1 Introduction

Gas-hydrate (GH) bearing sediments are partially frozen porous rocks with heterogeneities at mesoscopic scales. These sediments consist of a water phase and two non-welded solid phases, the skeleton and gas-hydrates, which are ice-like lattices of water molecules with gas methane trapped inside [1, 10]. These formations, found in permafrost and continental margins, are considered important future energy resources [1]. Their elastic properties and seismic velocities were analyzed by Lee and Collet [14, 15] and Carcione and Tinivella [4].

A theory to describe the static and dynamic behavior of partially frozen porous media was presented by Leclaire et al. [12], a generalization of the classic Biot theory to the case of two solids and one fluid. The theory, valid for uniform porosity, predicts the existence of additional compressional and shear waves which were observed in laboratory experiments [13]. Carcione and Seriani [3] designed a generalization of this theory to evaluate gas-hydrate concentration. Carcione et al. [6] and Santos et al. [17] generalized the theory of Leclaire et al. in [12] to the variable porosity case. In this generalization, the solid and GH matrices exchange kinetic and potential energy and the topology of the pores and grains is general, as that of Biot theory. Numerical simulations of wave propagation in partially frozen porous media were presented by Carcione and Seriani [5] and Carcione et al. [6]. We also refer to

✉ Jing Ba
jingba@188.com

1 School of Earth Sciences and Engineering, Hohai University, Nanjing, China

2 Universidad de Buenos Aires, Facultad de Ingeniería, Instituto del Gas y del Petróleo, Av. Las Heras 2214 Piso 3 C1127AAR, Buenos Aires, Argentina

3 Department of Mathematics, Purdue University, West Lafayette IN, USA

4 Departamento de Geofísica Aplicada, Facultad de Ciencias Astronómicas y Geofísicas, Universidad Nacional de La Plata, Paseo del Bosque s/n, La Plata, B1900FWA, Argentina

5 National Institute of Oceanography and Applied Geophysics OGS, Trieste, Italy

the Special Issue by Linga at al. [16] on gas hydrates and applications.

Seismic waves traveling through sediments with regions of different GH content suffer mode conversions at interfaces between those regions, generating wave-induced fluid flow (WIFF) in what it is known as the mesoscopic loss mechanism. This mechanism was first analyzed by White et al. [22] for the case of layered porous rocks saturated gas and water.

Among other authors working on the characterization of GH bearing sediments, we mention Waite et al. [21], whose theory is the classic Gassmann equation, where the fluids are mixed by using the Reuss average to obtain their bulk moduli, and do not consider the mesoscopic loss caused in thin layered media and/or patchy heterogeneities. On the other hand, Guerin and Goldberg [10] consider a composite model similar to that in Carcione et al. [6] and Santos et al. [17]. Their work provides some explanation of the attenuation on the basis of the squirt-flow model. Friction between minerals and ice is considered by using an empirical parameter and there is attenuation data from logs, but not from seismic data, a requirement to analyze the WIFF loss mechanism.

Even though in principle the generalized theory of Leclaire presented in [6] and [17] may be used to simulate wave propagation in highly heterogeneous gas-hydrate bearing sediments, a large number of degrees of freedom (DOF) would be required to properly represent the heterogeneities, i.e., extremely fine meshes. This in turn implies the solution of very large linear systems of equations, thus making such approach not feasible. As an alternative method, this work proposes the use of a numerical upscaling procedure allowing to determine an *effective viscoelastic medium* (EVM) that models the WIFF loss effect and behaves as a highly heterogeneous gas-hydrate bearing sediment.

The complex stiffnesses defining the EVM are obtained as solutions of boundary value problems (BVP's) for the quasi-static equations for composite materials derived in [17]. The BVP's impose boundary conditions associated with compressibility and shear experiments whose solutions are obtained with a finite-element (FE) procedure, so that the computer is used as a virtual laboratory. For a detailed description of using harmonic experiments combined with FE procedures to determine the seismic response of Biot-type media with different types of heterogeneities, we refer to [20]. The advantage of the proposed methodology consist of characterizing the seismic response of heterogeneous gas-hydrate bearing sediments with simple viscoelastic models. In particular, because of the reduction in DOF, this approach allows to define efficient computational algorithms to simulate wave propagation in this type of environments.

The organization of the paper is as follows. In Section 2, we present the model for GH bearing sediments. Section 3 is devoted to define the compressibility and shear experiments to determine a viscoelastic model long-wave equivalent to the original GH bearing sediment. Section 4 shows a collection of numerical experiments as follows. First, the procedure is validated for the homogeneous case against a classic Biot model as defined in Appendix B. Then, we analyze the WIFF mesoscopic loss mechanism in the inhomogeneous case: the isotropic case of patchy GH distributions, and periodic thin-layers of different GH content, leading to a anisotropic EVM (TI-EVM) representation of the original layered medium at long wavelengths. These media have not been measured experimentally yet.

2 The model

Let us consider an elementary cube Ω composed of two weakly-coupled porous solid phases, (sandstone and GH) referred to by the subscripts or superscripts 1 and 3, saturated by a single-phase fluid indicated by the subscript or superscript 2. Thus, $\Omega = \Omega_1 \cup \Omega_2 \cup \Omega_3$. The water content (effective porosity) and the two solid fractions over the bulk material are defined as $\phi_w = \frac{V_2}{V_b}$, $\phi_1 = \frac{V_1}{V_b}$ and $\phi_3 = \frac{V_3}{V_b}$, respectively, where $V_b = V_1 + V_2 + V_3$ and V_m is the volume of the phase Ω_m. The absolute porosity ϕ_a, corresponding to the case when the rock is completely unfrozen is $\phi_a = \phi_w + \phi_3 = 1 - \phi_1$. The GH content is defined as $I = \frac{\phi_3}{1-\phi_1}$, so that $0 \le I \le 1$.

Let $\boldsymbol{\tau}^{(1)} = \left(\tau_{ij}^{(1)}\right)$ and $\boldsymbol{\tau}^{(3)} = \left(\tau_{ij}^{(3)}\right)$ denote the stress tensors in Ω_1 and Ω_3 averaged over the bulk material Ω, respectively, and let p_f denote the fluid pressure. Also, let $\mathbf{u}^{(1)}$, $\mathbf{u}^{(2)}$ and $\mathbf{u}^{(3)}$ be the averaged solid and fluid displacements over the bulk material, while the relative fluid displacement is defined as

$$\mathbf{w} = \phi_w\left(\mathbf{u}^{(2)} - S_1\mathbf{u}^{(1)} - S_3\mathbf{u}^{(3)}\right), \tag{1}$$

with $S_1 = \frac{V_1}{V_1+V_3}$, $S_3 = \frac{V_3}{V_1+V_3}$ and $\zeta = -\nabla\cdot\mathbf{w}$ representing the change in fluid content.

Furthermore, let

$$\epsilon_{ij}(u^{(m)}) = \frac{1}{2}\left(\frac{\partial u_i^{(m)}}{\partial x_j} + \frac{\partial u_j^{(m)}}{\partial x_i}\right), \quad m = 1, 3,$$

denote the strain tensor in Ω_m with linear invariant $\theta_m = \epsilon_{ii}(u^{(m)})$. Also, the deviatoric strain tensor in Ω_m is

$$d_{ij}^{(m)} = \epsilon_{ij}(\mathbf{u}^m) - \frac{1}{3}\theta^{(m)}\delta_{ij}, \quad m = 1, 3.$$

The diffusion and constitutive equations for GH bearing sediments are derived in Santos et al. [17]:

$$\mathrm{i}\omega f_{11}\mathbf{u}^{(1)} - \mathrm{i}\omega f_{12}\mathbf{u}^{(2)} - \mathrm{i}\omega f_{11}\mathbf{u}^{(3)} = \nabla\cdot\boldsymbol{\tau}^{(1)}, \tag{2}$$

$$-\mathrm{i}\omega f_{12}\mathbf{u}^{(1)} + \mathrm{i}\omega f_{22}\mathbf{u}^{(2)} + \mathrm{i}\omega f_{12}\mathbf{u}^{(3)} = -\nabla p_f, \tag{3}$$

$$-\mathrm{i}\omega f_{11}\mathbf{u}^{(1)} + \mathrm{i}\omega f_{12}\mathbf{u}^{(2)} + \mathrm{i}\omega f_{11}\mathbf{u}^{(3)} = \nabla\cdot\boldsymbol{\tau}^{(3)}. \tag{4}$$

where ω is the angular frequency, $\mathrm{i} = \sqrt{-1}$ and

$$\tau_{ij}^{(1)} = \left[K_{G1}\theta_1 - B_1\zeta + B_3\theta_3\right]\delta_{ij} + 2\mu_1 d_{ij}^{(1)} + \mu_{1,3} d_{ij}^{(3)}, \tag{5}$$

$$\tau_{ij}^{(3)} = \left[K_{G3}\theta_3 - B_2\zeta + B_3\theta_1\right]\delta_{ij} + 2\mu_3 d_{ij}^{(3)} + \mu_{1,3} d_{ij}^{(1)}, \quad j,k = 1,2,3, \tag{6}$$

$$p_f = -B_1\theta_1 - B_2\theta_3 + K_{av}\zeta. \tag{7}$$

The determination of the elastic constants in Eqs. 5–7 and the diffusion coefficients f_{11}, f_{22} and f_{12} in Eqs. 2–4 is explained in Appendices A and B, respectively..

As already stated, to perform numerical simulations using Eqs. 2–4 it is necessary to employ extremely fine meshes to properly represent the mesoscopic-scale heterogeneities and their attenuation effects on the fast waves. As an alternative, we present in the next section a numerical upscaling procedures to determine the effective complex and frequency-dependent coefficients defining an EVM long-wave equivalent medium to the original Biot medium. We consider two cases, i.e., isotropic and finely layered (anisotropic) media, with the procedures yielding isotropic an anisotropic EVM, respectively.

3 The numerical upscaling procedure

3.1 The isotropic case. Experiments to determine the P- and S-wave complex moduli

Let us denote by $\mathcal{T}(\widetilde{\mathbf{u}}^s)$ and $\mathcal{E}(\widetilde{\mathbf{u}}^s)$ the time Fourier transforms of the stress and strain tensors of the isotropic EVM, and set $\widetilde{\Theta}^s = \nabla\cdot\widetilde{\mathbf{u}}^s$, where $\widetilde{\mathbf{u}}^s$ denotes the solid displacement vector. The constitutive equations of the EVM are

$$\mathcal{T}_{ij}(\widetilde{\mathbf{u}}^s) = \overline{\lambda}\widetilde{\Theta}^s\delta_{ij} + 2\overline{\mu}\mathcal{E}_{ij}(\widetilde{\mathbf{u}}^s). \tag{8}$$

To determine the complex and frequency dependent moduli $\overline{E_u} = \overline{\lambda} + 2\overline{\mu}$ and $\overline{\mu}$ in Eq. 8 we consider a square domain $\Omega = (0, L)^2$ in the (x_1, x_3)-plane with boundary $\Gamma = \Gamma^L\cup\Gamma^B\cup\Gamma^R\cup\Gamma^T$. Here Γ^L, Γ^R, Γ^T and Γ^B denote the left, right, top and bottom boundaries of Γ, respectively. Let $\{\boldsymbol{\nu}, \boldsymbol{\chi}\}$ be an orthonormal system on Γ, where $\boldsymbol{\nu}$ is the unit outer normal on Γ and $\boldsymbol{\chi}$ is a unit tangent on Γ oriented counterclockwise.

The complex modulus $\overline{E_u}$ is determined by solving Eqs. 2–4 in Ω with the boundary conditions

$$\boldsymbol{\tau}^{(m)}(\mathbf{u})\boldsymbol{\nu}\cdot\boldsymbol{\nu} = -\Delta P_m, \quad (x_1,x_3)\in\Gamma^T,\ m = 1,3, \tag{9}$$

$$\boldsymbol{\tau}^{(m)}(\mathbf{u})\boldsymbol{\nu}\cdot\boldsymbol{\chi} = 0, \quad (x_1,x_3)\in\Gamma,\ m = 1,3, \tag{10}$$

$$\mathbf{u}^{(m)}\cdot\boldsymbol{\nu} = 0, \quad (x_1,x_3)\in\Gamma\setminus\Gamma^T,\ m = 1,3, \tag{11}$$

$$\mathbf{w}\cdot\boldsymbol{\nu} = 0, \quad (x_1,x_3)\in\Gamma. \tag{12}$$

Note that the solution of this BVP satisfies the relations

$$\epsilon_{11}(\mathbf{u}^{(1)}) = \epsilon_{13}(\mathbf{u}^{(1)}) = \epsilon_{11}(\mathbf{u}^{(3)}) = \epsilon_{13}(\mathbf{u}^{(3)}) = \nabla\cdot\mathbf{w} = 0.$$

Thus, $\mathcal{E}_{11}(\widetilde{\mathbf{u}}^s) = \mathcal{E}_{13}(\widetilde{\mathbf{u}}^s) = 0$ and Eq. 8 reduces to

$$\mathcal{T}_{33} = \overline{E_u}\mathcal{E}_{33}. \tag{13}$$

Now $\overline{E_u}$ can be determined from Eq. 13 in terms of $\mathcal{T}_{33}$ and $\mathcal{E}_{33}$ as averages of the mesoscopic stress and strain tensors associated with the solid 1 phase over the sample Ω, i.e.,

$$\mathcal{T}_{33} = \frac{1}{\Omega}\int_\Omega \tau_{33}^{(1)}d\Omega, \qquad \mathcal{E}_{33} = \frac{1}{\Omega}\int_\Omega \epsilon_{33}^{(1)}d\Omega. \tag{14}$$

Next, the complex shear modulus $\overline{\mu}$ is determined by solving Eqs. 2–4 in Ω with the boundary conditions

$$-\boldsymbol{\tau}^{(1)}(\mathbf{u})\boldsymbol{\nu} = \mathbf{g}_1, \quad (x_1,x_3)\in\Gamma^T\cup\Gamma^L\cup\Gamma^R, \tag{15}$$

$$-\boldsymbol{\tau}^{(3)}(\mathbf{u})\boldsymbol{\nu} = \mathbf{g}_3, \quad (x_1,x_3)\in\Gamma^T\cup\Gamma^L\cup\Gamma^R, \tag{16}$$

$$\mathbf{u}^{(m)} = 0, \quad (x_1,x_3)\in\Gamma^B, \quad m = 1,3, \tag{17}$$

$$\mathbf{w}\cdot\nu = 0, \quad (x_1,x_3)\in\Gamma, \tag{18}$$

where

$$\mathbf{g}_1 = \begin{cases} (0,\Delta G_1), & (x_1,x_3)\in\Gamma^L,\\ (0,-\Delta G_1), & (x_1,x_3)\in\Gamma^R,\\ (-\Delta G_1,0), & (x_1,x_3)\in\Gamma^T, \end{cases} \tag{19}$$

$$\mathbf{g}_3 = \begin{cases} (0,\Delta G_3), & (x_1,x_3)\in\Gamma^L,\\ (0,-\Delta G_3), & (x_1,x_3)\in\Gamma^R,\\ (-\Delta G_3,0), & (x_1,x_3)\in\Gamma^T. \end{cases} \tag{20}$$

The solution of this BVP satisfies the conditions

$$\epsilon_{11}(\mathbf{u}^{(1)}) = \epsilon_{33}(\mathbf{u}^{(1)} = \epsilon_{11}(\mathbf{u}^{(3)}) = \epsilon_{33}(\mathbf{u}^{(3)}) = \nabla\cdot\mathbf{w} = 0,$$

and consequently $\mathcal{E}_{11}(\widetilde{\mathbf{u}}^s) = \mathcal{E}_{33}(\widetilde{\mathbf{u}}^s) = 0$. Hence, Eq. 8 reduces to

$$\mathcal{T}_{13} = \overline{\mu}\,\mathcal{E}_{13}. \tag{21}$$

Now $\overline{\mu}$ is obtained from Eq. 21 by computing $\mathcal{T}_{13}$ and $\mathcal{E}_{13}$ averaging the mesoscopic stress and strain tensors associated with the solid 1 phase over the sample Ω:

$$\mathcal{T}_{13} = \frac{1}{\Omega}\int_\Omega \tau_{13}^{(1)}d\Omega, \qquad \mathcal{E}_{13} = \frac{1}{\Omega}\int_\Omega \epsilon_{13}^{(1)}d\Omega. \tag{22}$$

The average bulk density of the sample is

$$\overline{\rho} = \phi_1\rho_1 + \phi_w\rho_2 + \phi_3\rho_3,$$

with $\rho_m, m = 1, 2, 3$ denoting the mass densities of the solid and fluid constituents in Ω. The complex compressional and shear velocities are [8]

$$v_{Pc}(\omega) = \sqrt{\frac{\overline{E_u}(\omega)}{\overline{\rho}}},\ v_{Sc}(\omega) = \sqrt{\frac{\overline{\mu}(\omega)}{\overline{\rho}}}.$$

The effective P and S phase velocities $v_n(\omega)$ and quality factors $Q_n(\omega), n = P, S$ are [8]

$$v_n(\omega) = \left[\mathrm{Re}\left(\frac{1}{v_{nc}(\omega)}\right)\right]^{-1}, \qquad \frac{1}{Q_n(\omega)} = \frac{\mathrm{Im}(v_{nc}^2(\omega))}{\mathrm{Re}(v_{nc}^2(\omega))}.$$

The approximate solution of the diffusion equations Eqs. 2–4 with the boundary conditions Eqs. 9–12 to determine $\overline{E_u}$ and Eqs. 15–18 to determine $\overline{\mu}$ is obtained with the FE method. See Santos et al. [18] for details on the application of the FE method to solve these type of harmonic experiments.

3.2 The anisotropic case. Periodic thin layers with dissimilar GH content

Finely layered media behaves as a TI-EVM at long wavelengths and five complex and frequency dependent stiffnesses $p_{IJ}(\omega)$ need to be determined. The constitutive equations for a TI-EVM are

$$\mathcal{T}_{11}(\widetilde{\mathbf{u}}_s) = p_{11}\,\mathcal{E}_{11}(\widetilde{\mathbf{u}}_s) + p_{12}\,\mathcal{E}_{22}(\widetilde{\mathbf{u}}_s) + p_{13}\,\mathcal{E}_{33}(\widetilde{\mathbf{u}}_s), \quad (23)$$
$$\mathcal{T}_{22}(\widetilde{\mathbf{u}}_s) = p_{12}\,\mathcal{E}_{11}(\widetilde{\mathbf{u}}_s) + p_{11}\,\mathcal{E}_{22}(\widetilde{\mathbf{u}}_s) + p_{13}\,\mathcal{E}_{33}(\widetilde{\mathbf{u}}_s), \quad (24)$$
$$\mathcal{T}_{33}(\widetilde{\mathbf{u}}_s) = p_{13}\,\mathcal{E}_{11}(\widetilde{\mathbf{u}}_s) + p_{13}\,\mathcal{E}_{22}(\widetilde{\mathbf{u}}_s) + p_{33}\,\mathcal{E}_{33}(\widetilde{\mathbf{u}}_s), \quad (25)$$
$$\mathcal{T}_{23}(\widetilde{\mathbf{u}}_s) = 2\,p_{55}\,\mathcal{E}_{23}(\widetilde{\mathbf{u}}_s), \quad (26)$$
$$\mathcal{T}_{13}(\widetilde{\mathbf{u}}_s) = 2\,p_{55}\,\mathcal{E}_{13}(\widetilde{\mathbf{u}}_s), \quad (27)$$
$$\mathcal{T}_{12}(\widetilde{\mathbf{u}}_s) = 2\,p_{66}\,\mathcal{E}_{12}(\widetilde{\mathbf{u}}_s), \quad (28)$$

where $p_{12} = p_{11} - 2p_{66}$.

Note that in finely layered media p_{33} and p_{55} can be identified with $\overline{E_u}$ and $\overline{\mu}$, respectively. Next, in order to analyze the behavior of waves traveling parallel to the layering ('11' waves), we define a new experiment to determine the stiffness p_{11}. This coefficient can be determined by solving Eqs. 2–4 in Ω with the boundary conditions

$$\boldsymbol{\tau}^{(m)}(\mathbf{u})\boldsymbol{\nu}\cdot\boldsymbol{\nu} = -\Delta P_m,\ (x_1, x_3) \in \Gamma^R,\ m = 1, 3, \quad (29)$$
$$\boldsymbol{\tau}^{(m)}(\mathbf{u})\boldsymbol{\nu}\cdot\boldsymbol{\chi} = 0,\ (x_1, x_3) \in \Gamma,\ m = 1, 3, \quad (30)$$
$$\mathbf{u}^{(m)}\cdot\boldsymbol{\nu} = 0,\ (x_1, x_3) \in \Gamma \setminus \Gamma^R,\ m = 1, 3, \quad (31)$$
$$\mathbf{w}\cdot\boldsymbol{\nu} = 0,\ (x_1, x_3) \in \Gamma. \quad (32)$$

The solution of this BVP for p_{11} satisfies

$$\epsilon_{33}(\mathbf{u}^{(1)}) = \epsilon_{12}(\mathbf{u}^{(1)}) = \epsilon_{33}(\mathbf{u}^{(3)}) = \epsilon_{12}(\mathbf{u}^{(3)}) = \nabla\cdot\mathbf{w} = 0,$$

so that $\mathcal{E}_{33}(\widetilde{\mathbf{u}}^s) = \mathcal{E}_{13}(\widetilde{\mathbf{u}}^s) = 0$ and Eq. 23 reduces to

$$\mathcal{T}_{11} = p_{11}\mathcal{E}_{11}. \quad (33)$$

Now, Eq. 33 determines p_{11} since $\mathcal{T}_{11}$ and $\mathcal{E}_{11}$ can be obtained as averages of the mesoscopic stress and strain tensors associated with the solid phase 1 over the sample, as indicated in Eq. 14 for determining p_{33}.

Numerical approximations to the complex coefficients $\overline{E_u}$ and $\overline{\mu}$ and p_{11} are computed with the FE method. See Santos and Gauzellino [20], Chapters 7 and 8, and also

Table 1 Material properties

Grain	bulk modulus, K_{s1}	38.7 GPa
	shear modulus, μ_{s1}	39.6 GPa
	density, ρ_{s1}	2650 kg/m^3
	permeability, κ_{s1}	1.07 10^{-13} m^2
Gas hydrate	bulk modulus, K_{s3}	8.58 GPa
	shear modulus, μ_{s3}	3.32 GPa
	density, ρ_{s3}	920 kg/m^3
	permeability, κ_{s3}	5 10^{-4} m^2
Water	bulk modulus, K_f	2.25 GPa
	density, ρ_2	1040 kg/m^3
	viscosity, η	0.0018 Pa · s

Table 2 Effective P-wave velocities (m/s) at 50 Hz as function of gas-hydrate content I

I	Composite model	classic Biot model	Error (%)
2/3	4120.23	4291.95	4.0
0.583	4064.18	4208.35	3.42
1/2	4027.02	4146.20	2.87
0.416	4004.44	4100.76	2.34
1/3	3992.67	4067.86	1.85
1/4	3988.48	4043.88	1.37
1/6	3989.24	4025.78	0.9

The sample is a square of side length 10 cm

Table 3 Effective S-wave velocities (m/s) at 50 Hz as function of gas-hydrate content I

I	Composite model	classic Biot model	Error (%)
2/3	2627.56	2639.26	0.44
0.583	2627.56	2572.36	0.28
1/2	2565.15	2526.03	0.16
0.416	2493.87	2495.93	0.08
1/3	2476.96	2477.85	0.03
1/4	2467.65	2467.95	0.01
1/6	2462.93	2462.99	0.0

The sample is a square of side length 10 cm

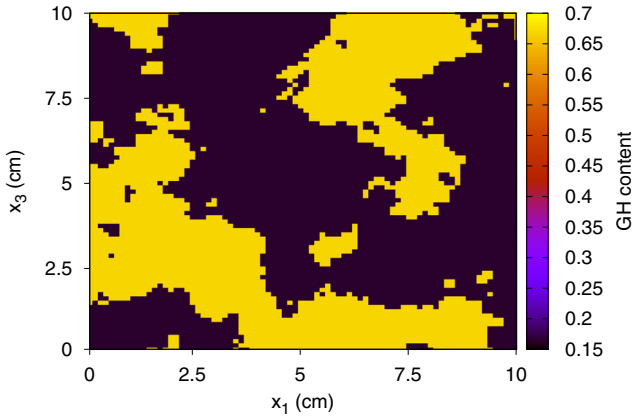

Fig. 1 Binary patchy gas-hydrate content I. Yellow regions have I = 2/3, black regions have I = 1/6. Correlation length is 3.33 cm. Overall gas-hydrate content is 36 %. The sample is a square of side length 10 cm

Santos et al. [18] and Santos and Carcione [19] for details on the implementation of the FE methods to determine complex stiffness in isotropic and anisotropic media.

4 Numerical experiments

4.1 Validation by comparison with the classic Biot model

There are no analytical solutions corresponding to the WIFF loss mechanism in composite porous media. We verify the methodology in the most complex case, where an analytical solution can be established for the wave velocity, but attenuation is negligible at seismic frequencies. We apply the tests to water saturated media. Then, the effective phase velocities v_n corresponding to the EVM, obtained with the harmonic experiments, are compared with those of the associated classic Biot model defined in Appendix B, which is long-wave

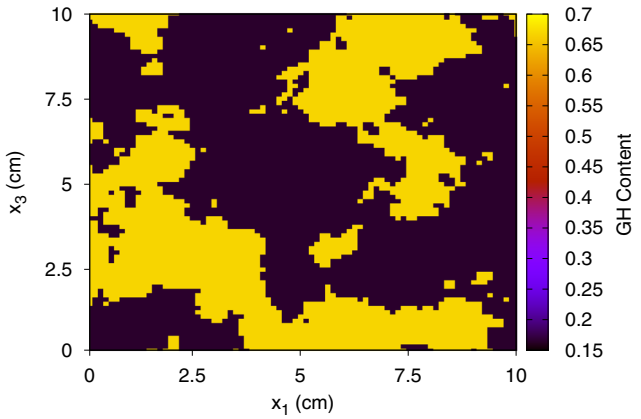

Fig. 2 Binary patchy gas-hydrate content I. Yellow regions have I = 2/3, black regions have I = 1/6. Correlation length is 2.22 cm. Overall gas-hydrate content is 36%. The sample is a square of side length 10 cm

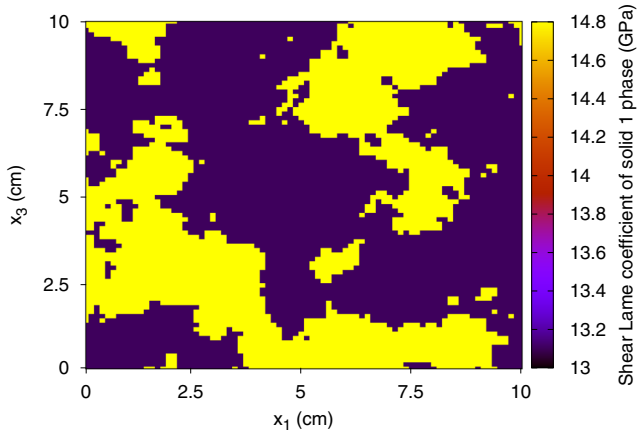

Fig. 3 Lamé shear coefficient μ_1 associated with the binary patchy gas-hydrate content of correlation length 2.22 cm in Fig. 2. Overall gas-hydrate content is 36%. The sample is a square of side length 10 cm

equivalent to the original composite model. Thus, we consider a water saturated homogeneous square sample of side length 10 cm discretized in a 80 × 80 uniform mesh. Absolute porosity is $\phi_a = 0.3$. The material properties of solid 1, solid 3 (GH) and water are given in Table 1. In all the examples, the mesh size is chosen so that the diffusion length is properly discretized. The validation is carried out by varying the GH content and as a function of frequency.

Table 2 shows the results for the effective P-wave phase velocities at 50 Hz varying the GH content. Its comparison with the values of the associated classic Biot model is displayed in the column of the percentual error. The error decreases with decreasing GH content. We consider that this is due to the very dissimilar elastic behavior of solids 1 and 3 (GH).

Furthermore, the effective P-wave velocities as a function of frequency for I = 1/3 were computed in the range 1 Hz-1 kHz (low-frequency range). We obtained an effective

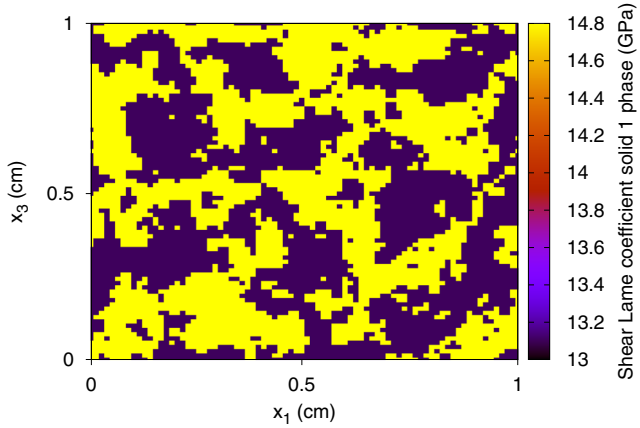

Fig. 4 Lamé shear coefficient μ_1 associated with a binary patchy gas-hydrate content of correlation length 0.04 cm and fractal dimension D = 2.2. Overall gas-hydrate content is 41%. The sample is a square of side length 1 cm

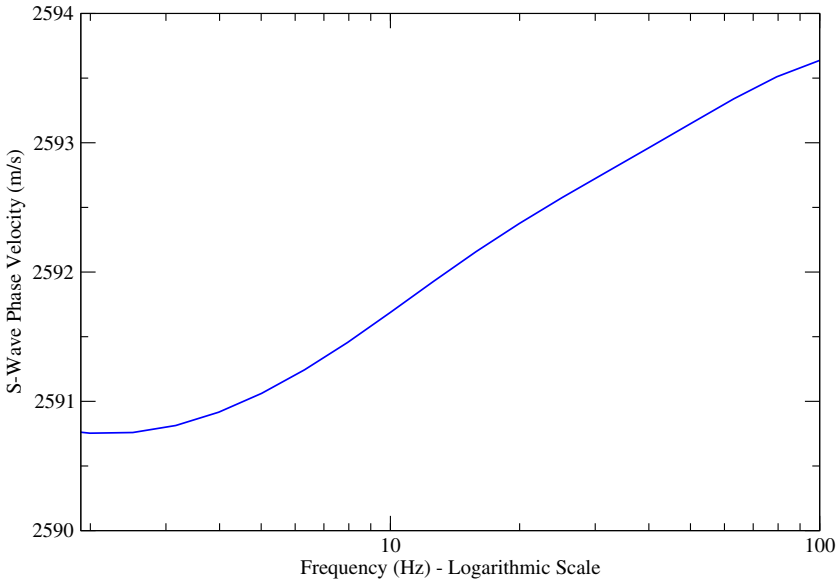

Fig. 5 Effective S-wave phase velocity as function of frequency for the composite model and a binary patchy gas-hydrate content of correlation length 0.04 cm and overall gas-hydrate content of 41%. The sample is a square of side length 1 cm

P-wave velocity of 3992.67 m/s and numerically an ∞ for the quality factor Q. We also computed the P-wave velocity for the associated classic Biot model defined in Appendix B using a plane-wave analysis, obtaining a constant of 4087.86 and dissipation factors in the range $10^{-2} - 10^{-5}$. Therefore, we verified that, at low frequencies, an homogeneous sample of the GH bearing sediment does not suffer attenuation and dispersion.

Table 3 presents the results for the effective S-wave phase velocities, showing – as for P-waves – that the errors decrease with decreasing GH content. We also computed the effective S-wave velocities as a function of frequency for I = 1/3. In the frequency range 1 Hz–1 kHz, we obtained an effective S-wave velocity of 2476.96 m/s and numerically an ∞ for the quality factor Q. The plane-wave analysis for the associated classic Biot model gives an S-wave phase velocity of 2477.85 m/s, while the dissipation factors are in the range $10^{-2} - 10^{-5}$. Similar results were obtained for different sample sizes.

4.2 Isotropic effective viscoelastic model for the case of patchy GH-content

Gas-hydrate bearing sediments have local variations in GH content I at multiple mesoscopic scales. To model wave propagation in this type of medium, a convenient approach is to use an isotropic EVM by solving the compressibility and shear experiments as defined in Section 3.1 using the FE method. This EVM takes into account WIFF and the associated dispersion and attenuation effects.

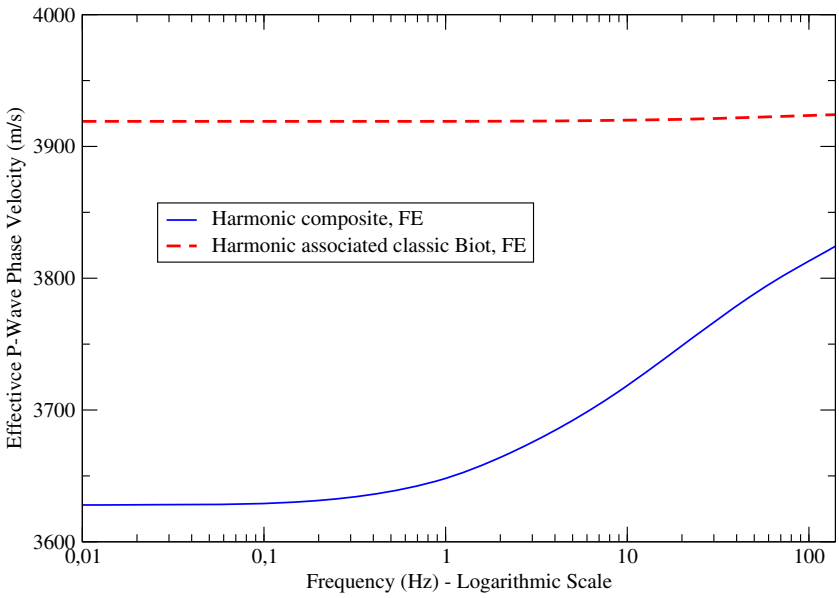

Fig. 6 Effective P-wave phase velocity as a function of frequency for the composite and classic Biot models and fractal binary gas-hydrate content I as in Fig. 2. Correlation length is 2.22 cm and overall gas-hydrate content is 36%. The sample is a square of side length 10 cm

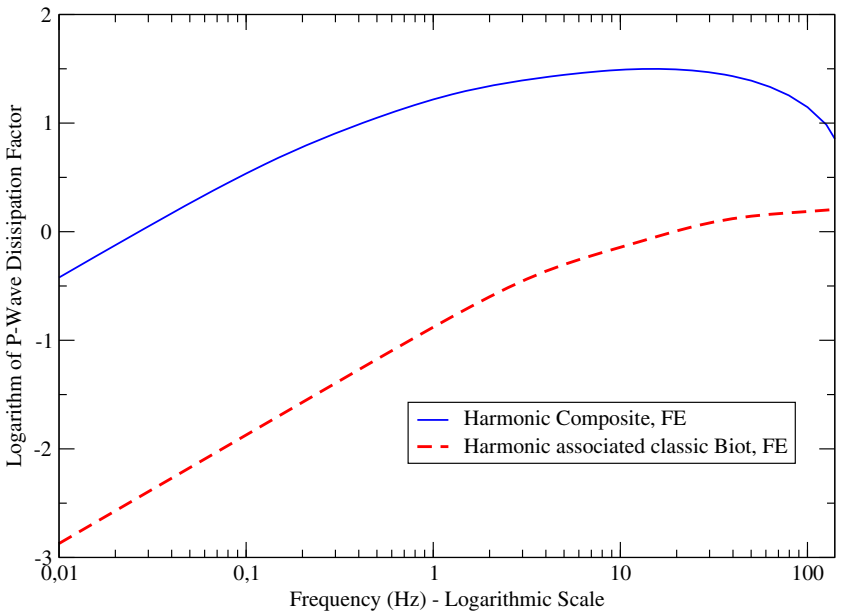

Fig. 7 Logarithm of effective P-wave dissipation factor as a function of frequency for the composite and classic Biot models and fractal binary gas-hydrate content I as in Fig. 2. Correlation length is 2.22 cm and overall gas-hydrate content is 36%. The sample is a square of side length 10 cm

The water-saturated sample Ω is a square of side length 10 cm discretized with a 80×80 uniform mesh. The binary multiscale quasi-fractal heterogeneities in GH content were generated with the von Karman self-similar correlation function [9]. The examples use a fractal dimension D =2.2 and two correlation lengths, 3.33 cm and 2.22 cm. For details on the procedure to generate these type of fractal distributions, we refer to Santos et al. [18].

Figures 1 and 2 display the patchy GH content distribution I for correlation lengths 3.33 cm and 2.22 cm, respectively. Overall the GH content I is 36%. Figure 3 shows the Lamé shear coefficient μ_1 associated with the patchy GH content distribution I in Fig. 2, where the local heterogeneities in μ_1 are due to local variations in the GH content. Fig. 4 shows the shear coefficient associated with a binary patchy gas-hydrate content of correlation length 0.04 cm, and Fig. 5 gives the effective S-wave phase velocity as function of frequency for the composite model.

Figures 6 and 7 show the effective phase velocities and logarithm of the dissipation factors of P waves as a function of frequency for the composite and classic Biot models in the range 0.01 Hz–140 Hz and binary GH content I as in Fig. 2 (correlation length 2.22 cm). The results for the classic Biot model were obtained with the FE upscaling procedure. The P-wave velocity for the composite model in Fig. 6 is lower than that of the classic Biot model, and shows a stronger dispersive behavior, while that of the classic Biot model is almost constant in all the frequency range. Figure 7

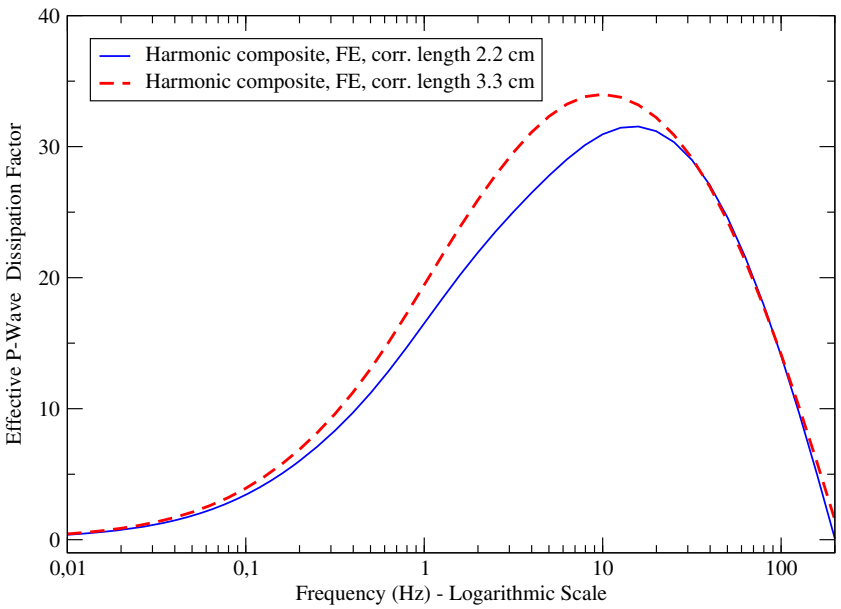

Fig. 8 Effective P-wave dissipation factor as a function of frequency for the composite model and fractal binary gas-hydrate content I as in Fig. 1 (correlation length is 3.33) and Fig. 2 (correlation length is 2.22). The attenuation peak moves to higher frequencies for the shorter correlation length. Overall gas-hydrate content is 36%. The sample is a square of side length 10 cm

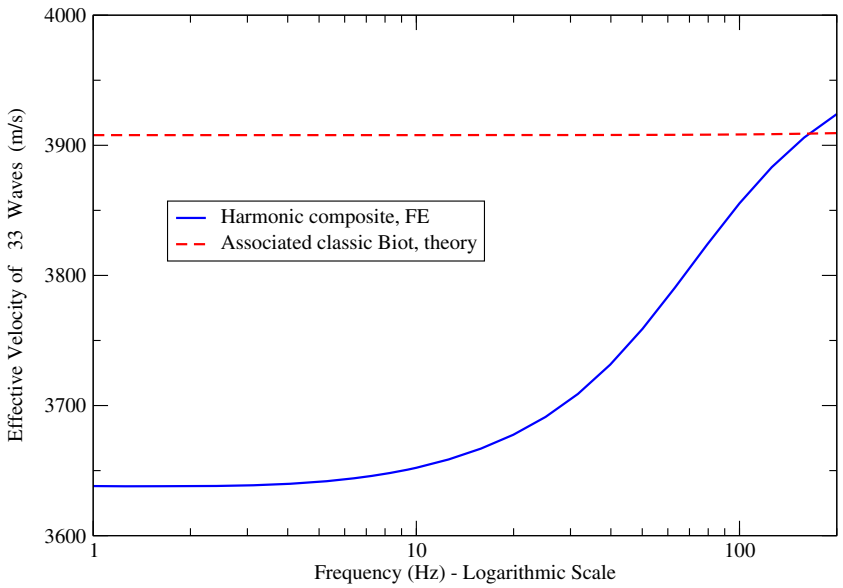

Fig. 9 Effective velocity of '33' waves as a function of frequency for the composite and classic Biot models. The numerical sample is a square of side length 18 cm and has six alternating layers of gas-hydrate contents I = 2/3 and 1/6

shows that the attenuation of the P waves is much higher for the composite model than for the classic Biot model. This attenuation mechanism, due to the induced WIFF effect, is not present when the latter model is used.

Figure 8 exhibits dissipation factors as a function of frequency for the composite model and the binary GH content distributions in Figs. 1 and 2. Two attenuation peaks are clearly observed. The peak located at lower frequencies corresponds to the larger GH patches (Fig. 1).

4.3 Shear waves in GH sediments with fractal patchy GH distribution

The next experiment analyzes the behavior of the shear waves as a function of frequency due to variations in GH content. In this case, the sample is a square of side length 1 cm with a multiscale quasi-fractal patchy GH distribution. The patches have a GH content I = 2/3 and I = 1/6. Absolute porosity is $\phi_a = 0.3$, correlation length is 0.04 cm and fractal dimension is D = 2.2. The overall GH content is 41%. Figure 4 displays the shear Lamé coefficient associated with this quasi-fractal GH distribution. It is observed that the S wave suffers very little velocity dispersion (see Fig. 5) and negligible attenuation. We also computed the corresponding effective phase velocity and dispersion coefficient of the classic Biot model, obtaining a constant shear phase velocity of 2428 m/s and negligible attenuation.

4.4 Effective viscoelastic model for the case of layered media with periodic variations in GH content

We consider a square sample of side length 18 cm discretized with a 120 × 120 uniform mesh. The numerical sample has six alternating layers of GH contents I = 2/3 and 1/6. Absolute porosity is $\phi_a = 0.3$.

First, we analyze waves traveling normal to the layers ('33' waves). The curves labeled *associated classic Biot* in the following Figures were obtained as follows. First, we determine the associated Biot model for each layer of the periodic sequence as indicated in Appendix B. Then, we use the theory given in Krzikalla and Müller [11] to obtain the theoretical values. The FE curves to determine p_{11} and p_{33} were computed by using the diffusion Eqs. 2–4 with the boundary conditions Eqs. 9–12, Eqs. 15–18 and Eqs. 29–32.]

Figure 9 exhibits effective '33'-wave velocities for the composite model increasing with increasing frequency, while those of the classic Biot model are almost constant in the whole frequency range. Furthermore, for almost all

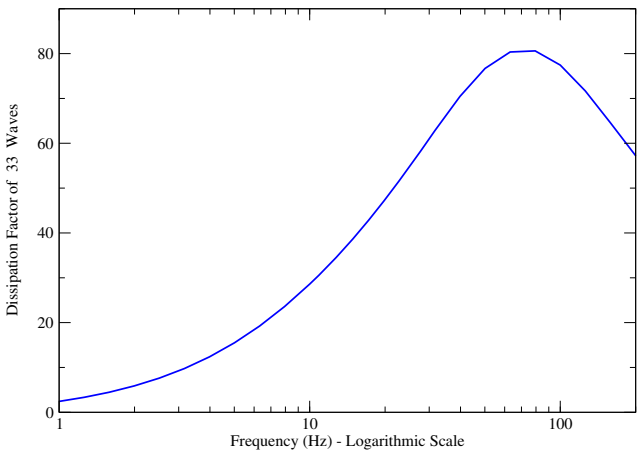

Fig. 10 Effective dissipation factor of '33' waves as a function of frequency for the composite model. The numerical sample is a square of side length 18 cm and has six alternating layers of gas-hydrate contents I = 2/3 and 1/6

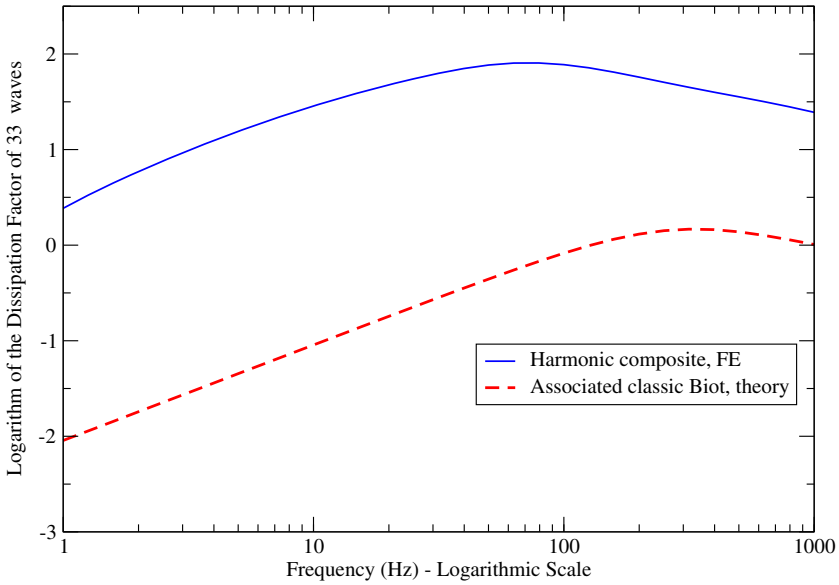

Fig. 11 Logarithm of the effective dissipation factor of '33' waves as a function of frequency for the composite and classic Biot models. The numerical sample is a square of side length 18 cm and has six alternating layers of gas-hydrate contents I = 2/3 and 1/6

frequencies, the composite model exhibits lower effective velocities than the classic model, due to the high dispersion induced by the WIFF mechanism. Figure 10 displays the effective '33'-wave dissipation factor of the composite model, where it can be observed high attenuation of P-waves due to the interlayer WIFF mechanism, with an attenuation peak of 80 for the dissipation factor at about 70 Hz. Figure 11 displays the logarithm of the dissipation factor of '33'-waves for the composite and classic Biot models, where attenuation is negligible for the latter model.

Figures 12 and 13 show the gradient of fluid pressure for the p_{33} experiment at 10 Hz and 70 Hz, where the higher values that can be observed at the interlayer boundaries are due to variations in GH content. These figures illustrate the WIFF mechanism. Furthermore, these gradients are much higher at 70 Hz than at 10 Hz, in accordance with Fig. 10.

Finally we analyze the behavior of '33' and waves traveling parallel to the layering plane, denoted in the Figures as '11' waves.

Figures 14 and 15 display effective phase velocities of '11' and '33' waves as function of frequency in the range 1Hz- 1kHz. In the range 1Hz- 100Hz, the associated classic Biot model predict that both waves have constant values of about 4170 m/s and 4167 m/s, respectively. After 100 Hz, velocities increase reaching values of 4189 m/s and 4181 m/s for '11' and '33' waves, respectively.

A completely different behavior is predicted by the effective comoposite model for both waves. '11' waves exhibit strong dispersion between 1Hz and 100Hz, with values of 3600 m/s at 1Hz and reaching with values of about 3925 m/s at 100 Hz, staying at that value until 1kHz. Concerning '33' waves, velocity stays at a constant value of

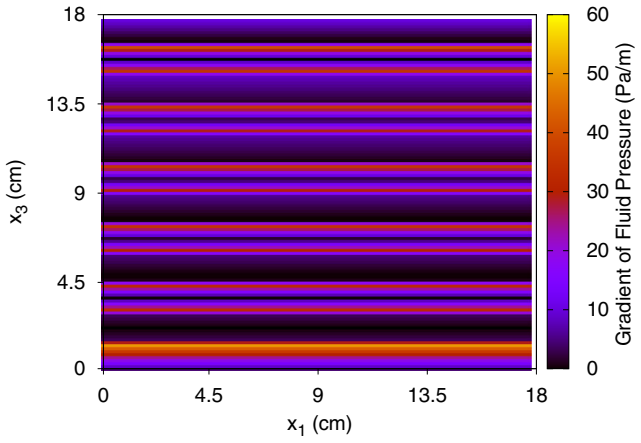

Fig. 12 Gradient of fluid pressure for compression normal to the layering (p_{33}-experiment) at 10 Hz for a square numerical sample of side length 18 cm and with six alternating layers of gas-hydrate contents I = 2/3 and 1/6

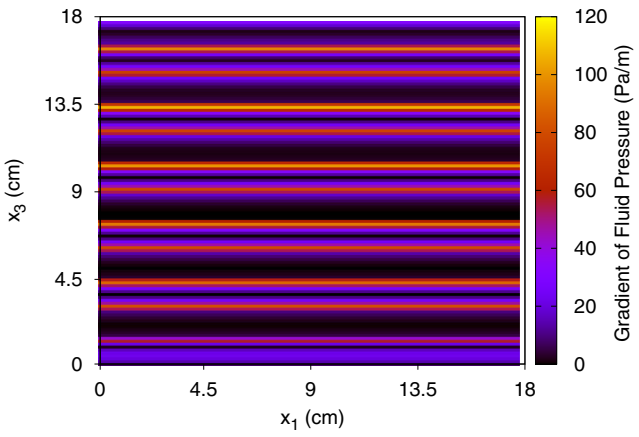

Fig. 13 Gradient of fluid pressure for compression normal to the layering (p_{33}-experiment) at 70 Hz for a square numerical sample of side length 18 cm with six alternating layers of gas-hydrate contents I = 2/3 and 1/6

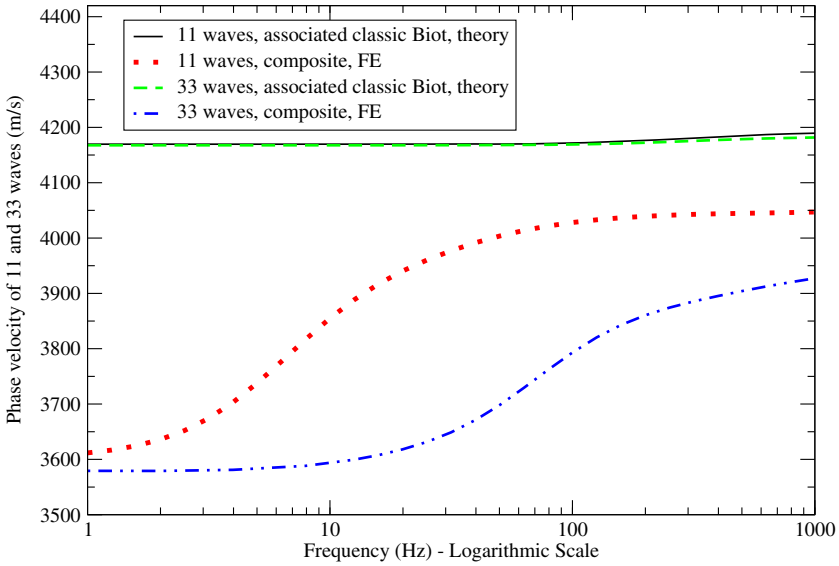

Fig. 14 Effective velocity of '11' and '33' waves as a function of frequency for the composite and classic Biot models computed using the FE method. The numerical sample is a square of side length 18 cm and has six alternating layers of gas-hydrate contents I = 2/3 and 1/6

about 3925 m/s between 1 and 10 Hz, afterwards showing strong dispersion with a value of 4046 at 1 kHz.

Figure 15 shows that dissipation factors are negligible for the classic Biot model with peaks at 300 Hz of approximate values 1000/6 and 1000/4 for '11' and '33' waves, respectively. On the other hand, attenuation predicted by the effective composite model is much higher, with Q-values of about 10 at 7 Hz for '11' waves and 12 at 70 Hz for '33' waves, respectively. The strong velocity dispersion and attenuation of '11' and '33' waves predicted by the effective composite model may be explained by the difference between the displacements of the two solid phases appearing in the diffusion coefficient f_{12} in Eq. 3, which induce energy dissipation not present in the associated classic Biot model.

5 Conclusions

We have developed a novel numerical upscaling technique for modeling the wave response of gas-hydrate bearing sediments. The procedure determines the complex and frequency dependent stiffness coefficients associated with an effective viscoelastic medium behaving as the original sediment. The modeling methodology uses an extension of Biot's theory, where the solid and fluid phases exchange kinetic and potential energy and exhibit dissipative behavior. Consequently, seismic waves exhibit mode conversions when traveling across interfaces between regions with different amounts of gas-hydrate, inducing the associated mesoscopic loss effect.

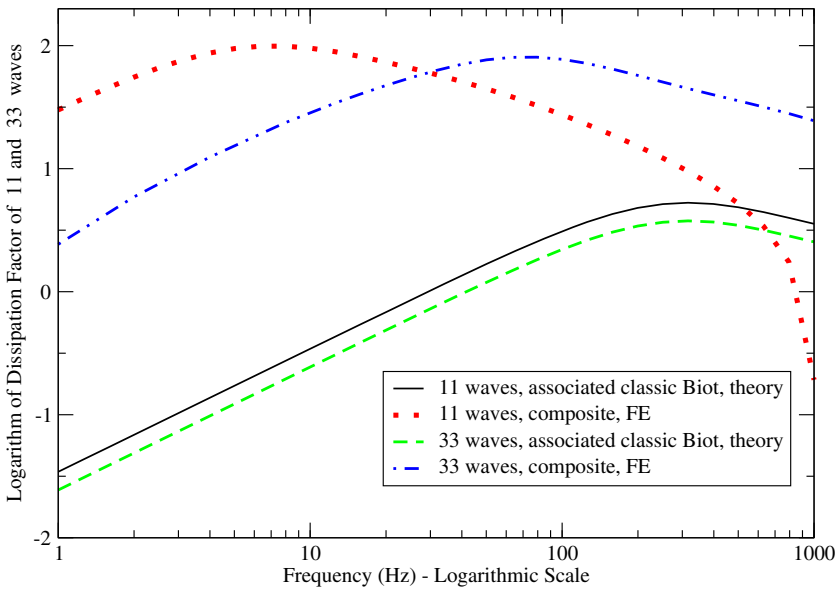

Fig. 15 Logarithm of dissipation factors of '11' and '33' waves a function of frequency for the composite and classic Biot models. computed using the FE method. The numerical sample is a square of side length 18 cm with six alternating layers of gas-hydrate contents I = 2/3 and 1/6

The numerical harmonic experiments allow us to estimate the stiffness coefficients of effective isotropic and anisotropic viscoelastic media that takes into account the wave-induced fluid-flow (mesoscopic) loss effect. This in turn allows us to implement simple and efficient computational algorithms to model wave propagation in heterogeneous sediments. The methodology is applied to study the seismic response of water saturated sediments with a patchy distribution of gas hydrate. The behavior of waves traveling normal and parallel to a periodic alternating horizontal layers with different amounts of gas-hydrate is also analyzed, based on an anisotropic representation of the original finely layered medium. The analysis shows that local variations in gas-hydrate content induce high velocity dispersion and attenuation of waves traveling normal or parallel to the layering, while the S waves are less sensitive to this type of heterogeneities.

Appendix A

The coefficients in the constitutive relations Eqs. 5–7 are computed as follows. Let $K_{s1,m}$, $K_{s3,m}$, $\mu_{s1,m}$ and $\mu_{s3,m}$ denote the bulk and shear modulus of the two solid (dry) frames, respectively. We assume that $K_{s1,m}$ is known and $K_{s3,m}$, $\mu_{s1,m}$ and $\mu_{s3,m}$ can be determined using a percolation-type model. See formulas A8-A9 of Appendix A in [17] for details. Then with K_{s1}, μ_{s1}, K_{s3} and μ_{s3} denoting the bulk and shear moduli of the grains in the two solid phases, respectively, and K_f the bulk modulus of the fluid phase, the coefficients μ_1, μ_3 and μ_{13} are:

$$\begin{aligned}
\mu_1 &= [(1-g_1)\phi_1]^2\mu_{av} + \mu_{s1,m}, \\
\mu_3 &= [(1-g_3)\phi_3]^2\mu_{av} + \mu_{s3,m}, \\
\mu_{13} &= (1-g_1)(1-g_3)\phi_1\phi_3\mu_{av}, \\
g_1 &= \frac{\mu_{s1,m}}{\phi_1\mu_{s1}}, \qquad g_3 = \frac{\mu_{s3,m}}{\phi_3\mu_{s3}}, \\
\mu_{av} &= \Big[\frac{(1-g_1)\phi_1}{\mu_{s1}} + \frac{\phi}{2\omega\eta} + \frac{(1-g_3)\phi_3}{\mu_{s3}}\Big]^{-1}.
\end{aligned} \tag{34}$$

The symbol ω in the definition of μ_{av} above denotes the angular frequency, taken to be $2\,\pi$ in the examples. The remaining elastic coefficients in Eqs. 5–7 are given by the following expressions [17]

$$\begin{aligned}
K_{G1} &= K_1 + (S_1)^2 K_2 + 2S_1 C_{12}, \\
K_{G3} &= K_3 + (S_3)^2 K_2 + 2S_3 C_{23}, \\
B_1 &= \frac{S_1 K_2 + C_{12}}{\phi}, \\
B_2 &= \frac{S_3 K_2 + C_{23}}{\phi}, \\
B_3 &= C_{13} + S_3 C_{12} + S_1 C_{23} + S_3 S_1 K_2,
\end{aligned} \tag{35}$$

$$K_{av} = \left[(1-c_1)\frac{\phi_1}{K_{s1}} + \frac{\phi}{K_f} + (1-c_3)\frac{\phi_3}{K_{s3}}\right]^{-1},$$

where

$$\begin{aligned}
K_1 &= [(1-c_1)\phi_1]^2\, K_{av} + K_{s1,m}, \\
K_2 &= \phi_w^2 K_{av} \\
K_3 &= [(1-c_3)\phi_3]^2\, K_{av} + K_{s3,m}, \\
C_{12} &= (1-c_1)\phi_1\phi K_{av}, \\
C_{13} &= (1-c_1)(1-c_3)\phi_1\phi_3 K_{av}, \\
C_{23} &= (1-c_3)\phi\phi_3 K_{av}, \\
c_1 &= \frac{K_{s1,m}}{\phi_1 K_{s1}}, \quad c_3 = \frac{K_{s3,m}}{\phi_3 K_{s3}}.
\end{aligned} \tag{36}$$

Appendix B

Here we describe a procedure to determine the dissipation factors of an associated classic Biot model that in the low-frequency range is *equivalent* to a composite material. The following notation is used to define the associated classic Biot model [2].

The solid and fluid particle displacements are denoted as $\widehat{\mathbf{u}}^{(s)}, \widehat{\mathbf{u}}^{(f)}$, while $\widehat{\boldsymbol{\sigma}}$ and $\widehat{p}_f$ denote the total stress and fluid pressure.

The constitutive relations and the diffusion equation of the classic Biot model are

$$\widehat{\sigma}_{ij} = \big[K_G\widehat{\theta}^{(s)} - B\widehat{\theta}^{(f)}\big]\delta_{ij} + 2\mu\widehat{d}_{ij}^{(s)}, \tag{37}$$

$$\widehat{p}_f = -B\widehat{\theta}^{(s)} - \widehat{K}_{av}\widehat{\theta}^{(f)}, \tag{38}$$

$$\nabla\cdot\widehat{\boldsymbol{\sigma}} = 0, \tag{39}$$

$$i\omega\frac{\eta}{\widehat{\kappa}}\widehat{\mathbf{u}}^{(f)} + \nabla p_f = 0, \tag{40}$$

where

$$\widehat{d}_{ij}^{(s)} = \epsilon_{ij}(\widehat{\mathbf{u}}^{s)}) - \frac{1}{3}\widehat{\theta}^{(s)}\delta_{ij}, \quad \widehat{\theta}^{(m)} = \nabla\cdot\widehat{\mathbf{u}}^{(m)}, m = s, f.$$

In Eqs. 37–40, K_G and μ are the bulk and shear moduli of the saturated material, while B and $\widehat{K}_{av}$ are elastic coupling coefficients. Furthermore, $\widehat{\kappa}$ denotes the rock permeability and η the fluid viscosity.

Let K_s^a, K_m^a, K_f denote the bulk moduli of the solid grains, dry matrix and fluid, respectively. The coefficient μ is the shear modulus of the dry matrix and the other coefficients in Eqs. 37–40 can be determined from the relations

$$K_G = K_m^a + \alpha^2\widehat{K}_{av}, \quad \alpha = 1 - \frac{K_m^a}{K_s^a}, \tag{41}$$

$$\widehat{K}_{av} = \left[\frac{\alpha-\phi_w}{K_s^a} + \frac{\phi_w}{K_f}\right]^{-1}, \quad B = \alpha\widehat{K}_{av}. \tag{42}$$

Assume that $\mathbf{u}^{(1)} = \mathbf{u}^{(3)} \equiv \mathbf{u}^{(s)}$ (the low-frequency assumption is used here) and define the total stress tensor as

$$\tau_{ij} = \tau_{ij}^{(1)} + \tau_{ij}^{(3)}. \tag{43}$$

Then adding Eqs. 5 and 6, we obtain

$$\tau_{ij} = \big[(K_{G1} + K_{G3} + 2\, B_3)\, \theta^{(s)} - (B_1 + B_2)\, \theta^{(f)} \big] \delta_{ij} + 2\, (\mu_1 + \mu_3 + \mu_{13})\, d_{ij}^{(s)}, \tag{44}$$

$$p_f = -(B_1 + B_2)\theta^{(s)} - K_{av}\theta^{(f)}. \tag{45}$$

Now from Eqs. 37, 38 and Eqs. 44, 45, we can identify the elastic coefficients of the associated classic Biot model as follows

$$K_G = K_{G1} + K_{G3} + 2\, B_3, \tag{46}$$

$$B = B_1 + B_2, \tag{47}$$

$$\mu = \mu_1 + \mu_3 + \mu_{13}, \tag{48}$$

$$\widehat{K}_{av} = K_{av}, \tag{49}$$

with the coefficients in the right-hand side of Eqs. 46– 49 computed by the relations given in Appendix A.

Next, note that we can determine α, K_m^a and K_s^a in Eqs. 41 and 42 as follows:

$$\alpha = \frac{B}{\widehat{K}_{av}}, \quad K_m^a = K_G - \alpha^2 \widehat{K}_{av} \quad K_s^a = \frac{K_m^a}{1-\alpha}, \tag{50}$$

where B, $\widehat{K}_{av}$ and K_G are given in terms of the coefficients of the GH-bearing sediments by Eqs. 46, 47 and 49, respectively.

The procedure to determine the coefficients K_G, B, $\widehat{K}_{av}$ and μ in Eqs. 46–49 can be shown to give identical results to those given in Carcione et al. [7]

Furthermore, from equations (B5) and (B8) in Santos et al. [17]

$$\phi_w\, (S_3 \phi_w f_{22} - f_{12}) = b_{23}, \tag{51}$$

$$\phi_w\, (f_{12} + S_1 \phi f_{22}) = b_{12}, \tag{52}$$

where

$$b_{12} = \phi_w^2 \frac{\eta}{\kappa_1}, \qquad b_{23} = \phi_w^2 \frac{\eta}{\kappa_3}, \tag{53}$$

with κ_1 and κ_3 denoting the permeabilities of two solid phases Thus, add Eqs. 51 and 52 to get

$$f_{22} = \eta \left(\frac{1}{\kappa_1} + \frac{1}{\kappa_3} \right). \tag{54}$$

Next, from the low-frequency assumption, the f_{12}-terms in Eq. 3 cancel and this equation reduces to

$$i\omega f_{22} \mathbf{u}^{(2)} + \nabla p_f = 0. \tag{55}$$

Thus Eqs. 40, 54 and 55 allow to identify the *effective* permeability $\widehat{\kappa}$ of the associated classic Biot model by the relation

$$\frac{1}{\widehat{\kappa}} = \left(\frac{1}{\kappa_1} + \frac{1}{\kappa_3} \right). \tag{56}$$

Equations 48 and 50 allow to determine the coefficients in Eqs. 41–42 in the constitutive relations of the the associated classic Biot medium to the GH-bearing sediment.

Remark Equations 46–49 and 56 may also be used in the case of shaley sandstones as presented in Santos et al. [17].

Acknowledgements This work was partially funded by ANPCyT, Argentina (PICT 2015 1909) and Universidad de Buenos Aires (UBACyT 20020160100088BA). The authors are grateful to the National Natural Science Foundation of China (Grant nos. 41974123) and the Jiangsu Province Outstanding Youth Fund Project (Grant no. BK20200021).

References

1. Ecker, C., Dvorkin, J., Nur, A.M.: Estimating the amount of gas hydrate and free gas from marine sediments. Geophysics **65**(2), 565–573 (2000)
2. Biot, M.A.: Mechanics of deformation and acoustic propagation in porous media. J. Appl. Phys. **33**, 1482–1498 (1962)
3. Carcione, J.M., Seriani, G.: Seismic velocities in permafrost. Geophys. Prosp. **46**, 441–454 (1998)
4. Carcione, J.M., Tinivella, U.: Bottom-simulating reflectors: Seismic velocities and AVO effects. Geophysics **65**(1), 54–67 (2000)
5. Carcione, J.M., Seriani, G.: Wave simulation in frozen porous media. J. Comput. Phys. **170**, 676–695 (2001)
6. Carcione, J.M., Santos, J.E., Ravazzoli, C.L., Helle, H.B.: Wave simulation in partially frozen porous media with fractal freezing conditions. J. Appl. Phys. **94**(12), 7839–7847 (2003)
7. Carcione, J.M., Helle, H.B., Santos, J.E., Ravazzoli, C.L.: A constitutive equation and generalized Gassmann modulus for multi-mineral porous media. Geophysics **70**(2), N17–N26 (2005)
8. Carcione, J.M.: Wave Fields in Real Media. Theory and numerical simulation of wave propa-gation in anisotropic, anelastic, porous and electromagnetic media, 3rd ed., extended and revised Elsevier Science Oxford (2014)
9. Frankel, A., Clayton, R.W.: Finite difference simulation of seismic wave scattering: implications for the propagation of short period seismic waves in the crust and models of crustal heterogeneity. J. Geophys. Res. **91**, 6465–6489 (1986)
10. Guerin, G.: Modeling of acoustic wave dissipation in gas-hydrate bearing sediments. Geochemistry, Geophysics, Geosystems 6 (7). https://doi.org/10.1029/2005GC000918 (2005)
11. Krzikalla, F., Müller, T.M.: Anisotropic p-SV-wave dispersion and attenuation due to interlayer flow in thinly layered porous rocks. Geophysics **76**, WA135 (2011). https://doi.org/10.1190/1.3555077
12. Leclaire, P., Cohen-Tenoudji, F., Aguirre Puente, J.: Extension of Biot's theory to wave propagation in frozen porous media. J. Acoust. Soc. Amer. **96**, 3753–3767 (1994)
13. Leclaire, P., Cohen-Tenoudji, F., Aguirre Puente, J.: Observation of two longitudinal and two transverse waves in a frozen porous medium. J. Acoust. Soc. Am. **97**, 2052–2055 (1995)
14. Lee, M.W., Collet, T.S.: Elastic properties of gas hydrate-bearing sediments. Geophysics **66**(3), 763–771 (2001)
15. Lee, M.W.: Biot-gassmann theory for velocities of gas hydrate-bearing sediments. Geophysics **67**(6), 1711–1719 (2002)
16. Linga, P., Clarke, M.A., Englezos, P.: Gas hydrates and applications. Part B **35**, 1353–1608 (2016)

17. Santos, J.E., Ravazzoli, C.L., Carcione, J.M.: A model for wave propagation in a composite solid matrix saturated by a single-phase fluid. J. Acoust. Soc. Am. **115**(6), 2749–2760 (2004)
18. Santos, J.E., Ravazzoli, C.L., Gauzellino, P.M., Carcione, J.M.: A numerical upscaling procedure to estimate effective bulk and shear moduli in heterogeneous fluid-saturated porous media. Comp. Methods Appl.Mech. Eng. **198**, 2067–2077 (2009)
19. Santos, J.E., Carcione, J.M.: Finite-element harmonic experiments to model fractured induced anisotropy in poroelastic media. Comp. Methods Appl.Mech. Eng. **283**, 1189–1213 (2015)
20. Santos, J.E., Gauzellino, P.M.: Numerical Simulation in Applied Geophysics. Lecture Notes in Geosystems Mathematics and Computing, Birkhauser (2017)
21. Waite, W.F., Santamarina, J.C., Cortes, D.D., Dugan, B., Espinoza, D.N., Germaine, J., Jang, J., Jung, J.W., Kneafsey, T.J., Shin, H., Soga, K., Winters, W.J., Yun, T.S.: Physical porperties of hydrate-bearing sediments. Rev. Geophys. **47**, RG4003 (2009). https://doi.org/10.1029/2008RG000279
22. White, J.E., Mikhaylova, N.G., Lyakhovitskiy, F.M.: Low-frequency seismic waves in fluid saturated layered rocks. Phys. Solid Earth **11**, 654–659 (1975)